Receptivity to Roughness, Acoustic, and Vortical Disturbances in Supersonic Boundary Layers Over Swept Wings

P. Balakumar and Rudolph A. King
Flow Physics and Control Branch
NASA Langley Research Center, Hampton, VA 23681

The receptivity and interaction of stationary and traveling crossflow instability of three-dimensional supersonic boundary layers over a swept biconvex wing with a blunt leading edge are numerically investigated for a freestream Mach number of 3. The steady and unsteady flow fields are obtained by solving the full Navier-Stokes equations. The receptivity of the boundary layer to surface roughness, freestream acoustic waves, and freestream vorticity waves are numerically investigated. The initial amplitudes of the stationary vortices generated by 1 μm roughness elements is about 2000 times larger than the initial amplitudes of the traveling disturbances generated by vortical disturbances with an amplitude level of $\tilde{u}_v/U_\infty = 1*10^{-5}$. The traveling crossflow vortices generated by acoustic disturbances of $\tilde{p}_{ac}/p_\infty = 1*10^{-5}$ are about 8 times weaker than the vortices generated by the vorticity waves. The interaction of stationary and traveling disturbances was investigated by solving the equations with both surface roughness and vortical disturbances. When the initial amplitudes of the stationary disturbances are large compared to the traveling disturbances, the stationary vortex dominates the perturbation field. When the amplitudes are comparable, the traveling vortex prevails and the stationary vortex is suppressed.

I. Introduction

Major technical challenges exist in achieving and maintaining laminar flow over swept wings. These challenges include the accurate prediction of the laminar-to-turbulent transition fronts and the ability to control the different boundary-layer instabilities that cause transition in these flows. These boundary-layer instabilities may include, but are not limited to, attachment-line, crossflow, and Tollmien-Schlichting instabilities. The transition of boundary layers in 'quiet' environments is first triggered by the exponential growth of small disturbances inside the boundary layer due to different linear instability mechanisms that exist for the boundary layer. Following the exponential growth, the final breakdown from laminar to turbulent flow occurs due to some nonlinear mechanisms. Hence, the transition onset from a laminar to turbulent state depends on (1) the initial amplitudes of different instability waves that are generated inside the boundary layer, (2) the growth rate of these different instability waves, and (3) the nonlinear mechanisms that cause the final breakdown. In this paper, we are concerned with the first two elements of the transition process in the supersonic three-dimensional boundary-layer flow over a swept wing.

Numerous studies have been conducted on the linear stability, nonlinear stability, and prediction of transition in three-dimensional boundary layers. Review articles by Arnal[1], Reed & Saric[2], Malik[3], Bippes[4] and Saric et al.[5] give comprehensive overviews of the various instability mechanisms and prediction capabilities. In the absence of attachment-line contamination, boundary-layer transition over swept wings near the leading edge is typically caused by the crossflow instability induced by spanwise pressure gradients. The crossflow instability is comprised of both three-dimensional traveling and stationary disturbances. The growth rates of the traveling disturbances are generally larger than those for

the stationary disturbances. The stationary crossflow vortices originate from three-dimensional roughness elements located near the leading edge of the wing where the boundary layer is thin. Traveling disturbances are generated by freestream acoustic and/or turbulent disturbances or by the interaction of freestream disturbances and surface roughness.

The importance of traveling versus stationary disturbances depends on the environmental conditions such as the surface finish and the unsteady freestream disturbance levels such as turbulence and acoustic, as these determine the initial amplitude values of the boundary-layer disturbances. Qualitatively, for a fixed surface finish one expects three different scenarios. (1) At small freestream disturbances, the initial amplitudes of the traveling disturbances are small and the transition will be dominated by the stationary disturbances. (2) At very high freestream disturbance levels, the initial amplitudes of the traveling disturbances are high, and since the growth rates of the traveling disturbances are larger than the growth rates for the stationary disturbances, the transition will be dominated by the traveling disturbances. (3) For medium freestream disturbance levels both the stationary and the traveling disturbances will have comparable initial amplitude levels and the transition will be influenced by both stationary and traveling disturbances.

The transition in swept wing incompressible flows caused by stationary crossflow vortices has been thoroughly investigated both experimentally and numerically.[4,5,6,7,8] The crossflow vortices originate from three-dimensional roughness elements located near the leading edge of the wing. After the vortices form, the amplitudes of the perturbations grow exponentially downstream due to linear instability and eventually saturate at values of approximately 20% of the boundary-layer edge velocity. These saturated vortices persist for long distances and appear as co-rotating vortices aligned very close to the local inviscid streamlines. These vortices lift the low momentum fluid from the wall region towards the outer edge of the boundary layer into regions of high-speed fluid. This produces highly inflectional velocity profiles in the streamwise and spanwise directions. These profiles become strongly unstable to high-frequency secondary instabilities. After the initiation of the secondary instability, the boundary layer breaks down to turbulence in a relatively short distance.

Bippes and colleaques[4] systematically investigated the effect of different environmental conditions on transition in incompressible flows over a swept flat plate with an imposed favorable pressure gradient. Experiments were conducted in two ways. In one case, the experiments were performed with a fixed surface roughness of $6 \mu m$ in three different tunnels with increasing turbulence levels of Tu = 0.08, 0.15 and 0.57%. In the other case, the experiments were performed with a fixed turbulence level of Tu = 0.15% with increasing roughness heights of 1.8, 6 and $10 \mu m$. The results of the experiment showed that when the initial amplitudes of the stationary disturbances are larger than the initial amplitudes for the traveling disturbances, the stationary disturbances dominate the transition. It was also observed that due to the large stationary vortices, the growth rates of the traveling disturbances are modified downstream. At moderate amplitude levels, the initial amplitudes of the stationary and traveling disturbances are in the same range and the traveling disturbances reach larger values compared to the stationary vortices. It was also observed that the traveling disturbances always reduce the growth of the stationary disturbances. At very high turbulence levels, the traveling disturbances dominate and the stationary disturbances decay in the downstream direction. In all the cases, the final breakdown takes place due to high-frequency secondary instabilities. Linear and nonlinear evolution of stationary and traveling waves in a swept Hiemenz flow were numerically investigated by Mujeeb et al.[6] using PSE (Parabolized Stability Equations) approach. The conclusions drawn from these calculations agree qualitatively with the experimental observations of Bippes[4].

In our previous paper[9], we numerically investigated the receptivity due to roughness, stability, and transition of three-dimensional supersonic boundary layers over (1) a swept cylinder, (2) a swept wing with a sharp leading edge, and (3) a swept wing with a blunt leading edge for a freestream Mach number of 3. These computations were performed for the same conditions as those in the experimental and computational study of Archambaud et al.[10] Receptivity computations for the flow over the swept cylinder showed that the roughness elements are less efficient in generating the stationary crossflow vortices when compared to the swept wings. The initial amplitudes of the nondimensional maximum

streamwise velocity for the stationary crossflow vortices originating from isolated 5μm roughness elements are $6.5*10^{-5}$, 0.02 and 0.015 for the flow over the cylinder, the sharp wing, and the blunt wing, respectively. The amplitudes of the crossflow vortices initially grow exponentially and eventually saturate further downstream. The approximate saturation amplitudes of the maximum streamwise velocity are 0.10, 0.12 and 0.18 for the three cases respectively. If we use these two amplitudes, the initial amplitudes and the saturation amplitudes, to compute the N-factors near the saturation point, the calculated N-Factors are about 7.3, 1.8 and 2.5 for the three cases. This, at least partially, explained the scatter in the computed N-Factor values at the experimentally observed transition onset points in Ref. 10.

The first objective of this study was to compute the receptivity coefficients for (1) the stationary crossflow vortices that originate from three-dimensional roughness elements, (2) the traveling crossflow vortices generated by freestream acoustic disturbances, and (3) the traveling crossflow vortices generated by freestream vortical disturbances. After the receptivity computations were performed, we investigated the second objective that involved the interaction of traveling and stationary disturbances. These computations were performed for a fixed roughness height of 1μm with increasing freestream turbulence levels of $1.0*10^{-4}$, $1.0*10^{-3}$ and $1.0*10^{-2}$. The simulations were performed by solving the three-dimensional Navier-Stokes equations using a 5th-order accurate weighted essentially non-oscillatory (WENO) scheme for space discretization and using a 3rd-order, total variation diminishing (TVD) Runge-Kutta scheme for time integration. Computations were performed for supersonic flow over a blunt swept wing. The reference configuration and test conditions are as those reported in Ref. 10.

This paper is organized in the following manner. A brief discussion about the solution procedure and governing equations are discussed in section II. Results that include mean flow profiles, linear stability analysis, receptivity coefficients, evolution of stationary and traveling disturbances originating from surface roughness and freestream disturbances, and interaction of crossflow vortices originating from roughness elements and vortical disturbances are presented in section III. And finally, conclusions are drawn in section IV.

II. Formulation of the problem

We consider supersonic flow over an infinite swept wing with a blunt leading edge (Fig. 1). The Cartesian coordinates, (*x, y, z*), are oriented such that *x* is along the chord direction perpendicular to the leading edge, *z* is along the spanwise direction and *y* is along the normal direction. The sweep angle is *Λ*, the freestream Mach number is *M* and the freestream velocity is q_∞. We are interested in the stationary and traveling crossflow instability dominated transition in three-dimensional supersonic boundary layers. Stationary crossflow vortices originate from three-dimensional isolated roughness elements. The traveling crossflow vortices are generated by the interaction of freestream acoustic and/or turbulent fluctuations with the boundary layer. Our approach is to investigate the influence of the surface roughness, freestream acoustic disturbances and freestream turbulent disturbances on the generation of instability waves separately. After the individual effects are identified, we investigate the interactions of the disturbances generated by roughness and turbulence for a fixed roughness height with increasing turbulence levels.

A. Roughness.

We consider a three-dimensional, spanwise-periodic roughness strip placed on the surface of the wing very close to the leading-edge region near the neutral point. The shape of the roughness is in the form

$$y_c(x,z) = h\, e^{-\sigma\left(\frac{x-x_r}{\Delta x}\right)^2} \cos\beta z. \tag{1}$$

Here y_c is the height of the roughness normal to the surface of the wing, h is the maximum height, x_r is the surface location of the roughness, Δx is related to the spatial extent of the roughness along the wing, β is the spanwise wave number, and σ is a constant that determines the width of the roughness in the x-direction.

B. Plane Acoustic and Vorticity waves.

The linearized Euler equations in Cartesian coordinates in a uniform mean flow are:

$$\frac{\partial \rho}{\partial t} + U_0 \frac{\partial \rho}{\partial x} + \rho_0 \frac{\partial u}{\partial x} + V_0 \frac{\partial \rho}{\partial y} + \rho_0 \frac{\partial v}{\partial y} + W_0 \frac{\partial \rho}{\partial z} + \rho_0 \frac{\partial w}{\partial z} = 0,$$

$$\rho_0 \frac{\partial u}{\partial t} + \rho_0 U_0 \frac{\partial u}{\partial x} + \rho_0 V_0 \frac{\partial u}{\partial y} + \rho_0 W_0 \frac{\partial u}{\partial z} = -\frac{\partial p}{\partial x},$$

$$\rho_0 \frac{\partial v}{\partial t} + \rho_0 U_0 \frac{\partial v}{\partial x} + \rho_0 V_0 \frac{\partial v}{\partial y} + \rho_0 W_0 \frac{\partial v}{\partial z} = -\frac{\partial p}{\partial y},$$

$$\rho_0 \frac{\partial w}{\partial t} + \rho_0 U_0 \frac{\partial w}{\partial x} + \rho_0 V_0 \frac{\partial w}{\partial y} + \rho_0 W_0 \frac{\partial w}{\partial z} = -\frac{\partial p}{\partial z},$$

$$\rho_0 c_p \frac{\partial T}{\partial t} + \rho_0 U_0 c_p \frac{\partial T}{\partial x} + \rho_0 V_0 c_p \frac{\partial T}{\partial y} + \rho_0 W_0 c_p \frac{\partial T}{\partial z} = \frac{\partial p}{\partial t} + U_0 \frac{\partial p}{\partial x} + V_0 \frac{\partial p}{\partial y} + W_0 \frac{\partial p}{\partial z},$$

$$P_0 = \rho_0 R T_0,$$

$$p = \rho_0 R T + \rho R T_0.$$

$$(2)$$

(a) Acoustic waves.

The solution of this system for the acoustic waves can be written as

$$\begin{Bmatrix} \rho \\ u \\ v \\ w \\ T \end{Bmatrix} = \begin{Bmatrix} \dfrac{1}{a_0^2} \\ -\dfrac{\alpha_{ac}}{\rho_0(\alpha_{ac}U_0 + \varepsilon_{ac}V_0 + \beta_{ac}W_0 - \omega)} \\ -\dfrac{\varepsilon_{ac}}{\rho_0(\alpha_{ac}U_0 + \varepsilon_{ac}V_0 + \beta_{ac}W_0 - \omega)} \\ -\dfrac{\beta_{ac}}{\rho_0(\alpha_{ac}U_0 + \varepsilon_{ac}V_0 + \beta_{ac}W_0 - \omega)} \\ \dfrac{(\gamma-1)T_0}{\rho_0 a_0^2} \end{Bmatrix} p. \tag{3}$$

Here the pressure p is in the form

$$p = p_{amp} e^{i(\alpha_{ac}x + \varepsilon_{ac}y + \beta_{ac}z - \omega t)}. \tag{4}$$

The dispersion relation among the wavenumbers α_{ac}, β_{ac}, ε_{ac} and the frequency ω is given by

$$(\alpha_{ac}U_0 + \varepsilon_{ac}V_0 + \beta_{ac}W_0 - \omega)^2 = (\alpha_{ac}^2 + \beta_{ac}^2 + \varepsilon_{ac}^2)a_0^2.$$ (5)

(b) Vorticity waves.

The solution of the linearized Euler equations for the vorticity waves can be written as

$$\begin{Bmatrix} \rho \\ u \\ v \\ w \\ T \end{Bmatrix} = \begin{Bmatrix} 0 \\ \tilde{u} \\ \tilde{v} \\ \tilde{w} \\ 0 \end{Bmatrix} e^{i(\alpha_v x + \varepsilon_v y + \beta_v z - \omega t)}.$$ (6)

The dispersion relation among the wavenumbers α_v, β_v, ε_v and the frequency ω is given by

$$(\alpha_v U_0 + \varepsilon_v V_0 + \beta_v W_0 - \omega) = 0.$$ (7)

The continuity equation imposes the following constraint on the velocity components

$$\tilde{u}\alpha_v + \tilde{v}\varepsilon_v + \tilde{w}\beta_v = 0.$$ (8)

C. Governing Equations.

The equations solved are the three-dimensional unsteady compressible Navier-Stokes equations in conservation form

$$\frac{\partial}{\partial t}Q_i + \frac{\partial}{\partial x_j}\left(F_{ji} - F_{vji}\right) = 0 ,$$ (9)

where $$Q_i = \begin{Bmatrix} \rho \\ \rho E \\ \rho u \\ \rho v \\ \rho w \end{Bmatrix}, \quad \left[F_{ji}\right] = \begin{Bmatrix} \rho u_j \\ (\rho E + p)u_j \\ \rho u u_j + \delta_{1j}p \\ \rho v u_j + \delta_{2j}p \\ \rho w u_j + \delta_{3j}p \end{Bmatrix}, \quad \left[F_{vij}\right] = \begin{Bmatrix} 0 \\ u\tau_{1j} + v\tau_{2j} + w\tau_{3j} - q_j \\ \tau_{1j} \\ \tau_{2j} \\ \tau_{3j} \end{Bmatrix},$$ (10)

(x, y, z) are the Cartesian coordinates, (u, v, w) are the velocity components, ρ is the density, and p is the pressure. E is the total energy per unit mass given by

$$E = e + \frac{u^2 + v^2 + w^2}{2},$$

$$e = c_v T, \quad p = \rho RT$$ (11)

where e is the internal energy per unit mass and T is the temperature. The shear stress and the heat flux are given by

$$\tau_{ij} = \mu \left\{ \frac{\partial u_i}{\partial x_j} + \frac{\partial u_j}{\partial x_i} - \frac{2}{3} \delta_{ij} \frac{\partial u_k}{\partial x_k} \right\}, \quad q_j = -k \frac{\partial T}{\partial x_j}. \tag{12}$$

The viscosity, μ, is computed using Sutherland's law and the coefficient of conductivity, k, is given in terms of a constant Prandtl number, Pr. The variables ρ, p, T and velocity are non-dimensionalised by their corresponding reference variables ρ_∞, p_∞, T_∞ and $\sqrt{RT_\infty}$, respectively. The subscript "∞" denotes freestream quantities. Additionally, q_∞ is defined as the freestream velocity and y_n is the local wall-normal coordinate. For the computation, the equations are transformed from the physical coordinate system (x, y, z) to the computational curvilinear coordinate system (ξ, η, ζ) in a conservative manner.

(a) Solution Algorithm.

The governing equations are solved using a 5th-order accurate weighted essentially non-oscillatory (WENO) scheme for space discretization and using a 3rd-order, total variation diminishing (TVD) Runge-Kutta scheme for time integration. These methods are suitable in flows with discontinuities or high gradient regions. The governing equations are solved discretely in a uniform structured computational domain where flow properties are known point wise at the grid nodes. In a given direction, the spatial derivatives are approximated to a higher order at the nodes, using the neighboring nodal values in that direction. The resulting equations are then integrated in time to get the point values as a function of time. Since the spatial derivatives are independent of the coordinate directions, multi dimensions can be easily added to the method. It is well known that approximating a discontinuous function by a higher-order (two or more) polynomial generally introduces oscillatory behavior near the discontinuity, and this oscillation increases with the order of the approximation. The essentially non-oscillatory (ENO) and the improved WENO methods were developed to maintain the higher-order approximations in the smooth regions and to eliminate or suppress the oscillatory behavior near the discontinuities. These objectives are achieved by systematically adopting or selecting the stencils based on the smoothness of the function that is being approximated. Shu[11] explains the WENO and the TVD methods and the formulas. Atkin[12] gives the application of the ENO method to the Navier-Stokes equations. Balakumar et al.[13] describe in detail the solution method implemented in this computation.

At the outflow boundary, extrapolation is used to obtain the flow variables. At the wall, no-slip conditions are used for the velocities and a constant temperature condition is employed for the temperature. The density at the wall is computed from the continuity equation. In the spanwise direction, periodic conditions are imposed at the boundaries. The freestream values are prescribed at the upper boundary that lies outside the bow shock and simulations are performed using a variable time step until the maximum residual reaches a small value on the order of 10^{-11}. A CFL number of 0.5 is used in these computations.

The grid stretches in the η direction close to the wall and is uniform outside the boundary layer. In the ξ direction, the grid is symmetric about the nose and is very fine near the nose and becomes uniform in the flat region. The grid is uniform in the spanwise ζ direction. The outer boundary outside of the shock follows a parabola where the vertex is located a short distance upstream of the nose to capture the boundary layer accurately.

III. Results

The computations are performed for supersonic flows over a swept wing with a blunt leading edge at zero angle of attack. Figure 1 shows the schematic diagram of the computational set up. Simulations are conducted for the reference configuration and flow parameters tested in Ref. 10. The airfoil is a biconvex shape with a constant curvature radius. The chord length is 150 mm and the maximum thickness is 30

mm. A parabola with a leading-edge radius of 6 mm models the leading edge of the wing. The flow parameters and the dimensions are given in Table 1. The transition onset location in the experiment[10] for the flow parameters in the table occurred at $x = 45$ mm from the leading edge. The computational domain extends from $x = -10$ to 55.0 mm in the axial direction. Calculations are performed using a grid size of (1501*251*41).

Table 1. Flow parameters for the blunt swept wing model

Chord length: $C = 150$ mm

Maximum thickness: $t = 30$ mm

Freestream Mach number: $M_\infty = 3.0$

Sweep angle: $\Lambda = 30$ degrees

Freestream Reynolds number: $Re_\infty = 18.0 \times 10^6$/m.

Freestream temperature: $T_\infty = 121.42 \, °K$

Wall temperature: $T_w = 300.0 \, °K$

Prandtl number: $Pr = 0.70$

Ratio of specific heats: $\gamma = 1.4$

Length scale: $\sqrt{\dfrac{\nu_\infty x_0}{q_\infty}} = 2.88 \times 10^{-2}$ mm ($x_0 = 15.0$ mm)

Non–dimensional frequency $F = 1 \times 10^{-5}$ is equivalent to $f = 19.0$ kHz

The non-dimensional frequency F is defined as $F = \dfrac{2\pi \nu_\infty f}{q_\infty^2}$,

where f is the frequency in Hertz.

A. Mean flow.

Figure 2 shows the density contours obtained from the Navier-Stokes simulation. The normal Mach number is 2.60. Due to the blunt leading edge, the shock is detached from the nose a distance of 2.8 mm. Figure 3(a) depicts the computed pressure and crossflow Reynolds number distributions along the wing. The computed pressure distribution agrees with the results obtained from Newton's law that is given in Ref. 10. The crossflow Reynolds number increases to about 250 at 5% of the chord. After 5% of the chord, the crossflow Reynolds number increases gradually at a near linear rate. The crossflow Reynolds number is about 400 near the transition onset location, $x = 45$ mm. Figure 3(b) displays the crossflow velocity profiles at different axial locations ($x = 1, 5, 10, 20$ and 40 mm). The boundary-layer thickness gradually increases from 0.075 mm at $x = 1.0$ mm to 0.50 mm at $x = 40$ mm. The maximum crossflow velocity remains at almost a constant value of approximately 0.07 starting from the leading edge.

B. Linear instability.

Figure 4 shows the N-factor results obtained from the local stability and linear PSE calculations for the traveling and the stationary disturbances. Computations were performed for a constant spanwise wavelength and include curvature effects. The linear stability results show that the N-factors at the observed transition onset location[10], $x = 45$ mm, are about 6.5 for the traveling disturbances and about 4.8

for the stationary disturbances. The frequency and spanwise wavelength of the most amplified traveling wave are about 40 kHz and 1.25 to 1.5 mm, respectively. The spanwise wavelength of the most amplified stationary disturbances is about 1.00 mm to 1.25 mm. The N-factors obtained from linear PSE computations based on u_{max} are 8.0 and 6.2 for the most amplified traveling and stationary disturbances, respectively. The streamwise wavelengths for the neutral instability waves and the freestream acoustic and vortical waves are listed in Table 2 for the two spanwise wavelengths of 1.00 and 1.25 mm. The corresponding neutral points for the stationary and traveling waves for the frequency of 40 kHz are also given in the Table 2. It is seen that the wavelengths of the slow acoustic waves, 8.20 and 11.80 mm, are much larger than that of the neutral instability waves, 1.49 and 2.22 mm, respectively. The wavelengths of the vortical waves, 1.96 and 2.53 mm, are still larger than that of the neutral waves but relative to the acoustic waves they are comparable to the neutral waves. We want to point out that the wavenumbers of all the waves presented in Table 2 (acoustic, vortical and linear stability) are negative. This implies that the trace velocities of the waves are propagating in the direction opposite to the chord.

Table 2. Neutral point locations and streamwise wavelengths of the stability waves at the neutral points and the streamwsie wavelengths of the acoustic and the vorticity waves in the freestream

	Neutral Points (mm)		Wavelenghts (mm)	
	$\lambda_z = 1.00$	$\lambda_z = 1.25$	$\lambda_z = 1.00$	$\lambda_z = 1.25$
0 Hz	2.74	3.52	1.14	1.53
40 kHz	2.46	3.36	1.49	2.22
Acoustic			8.20	11.80
Vortical			1.96	2.53

C. Roughness.

We performed direct numerical simulations with roughness elements placed near the neutral point. The parameters x_r, Δx, h and σ are given in Table 3. The boundary-layer thickness near $x = 1.0$ mm is about 0.075 mm. Simulations are performed for the most amplified waves with spanwise wavelengths $\lambda_z = 2\pi/\beta = 1.0$ mm and 1.25 mm for roughness heights, h, of 1μm. The roughness Reynolds number, $Re_{h,u} = |u|_h h/\nu_h$, for these parameters is about 0.6.

Table 3. Location and the height of the roughness on the blunt swept wing

x_r (mm)	h (mm)	σ	Δx(mm)	h/δ	Re$_{hu}$
1	0.001	3	0.25	1/75	0.6

Figure 5 depicts the contours of the u velocity at near half the boundary-layer height (y~0.05 mm) in the plan view (x, z) plane for the case $x_r = 1.0$ mm, $\lambda_z = 1.25$ mm and $h = 0.001$ mm. These are the footprints of the stationary crossflow vortices that originate from the roughness elements. Figure 6 displays the u-velocity contours in the cross-sectional planes (z, y) at different stations $x = 10.28$, 13.96,

23.50 and 31.60 mm along the wing. The crossflow vortices amplify downstream and develop strong shear layers in both the normal and the spanwise directions.

Figures 7(a) and (b) show the perturbations of the maximum u velocity in the $z = 0$ plane generated by the roughness elements for the $\lambda_z = 1.00$ mm case in linear and log scales, respectively. We also included the amplitude of the perturbations computed using linear PSE. The agreement is very good in the linear region and the computations from the linear theory deviate when the maximum u-velocity perturbations reach about 0.18. This is equivalent to 0.28 when it is non-dimensionalised by the boundary-layer edge velocity. The growth rate deviates from the linear theory near $x = 20$ mm and the amplitude of the vortices saturates at about $x = 25$ mm. We calculated the initial amplitude and the receptivity coefficients for the crossflow vortices that are generated by the roughness. The initial amplitudes of the instability waves near the neutral points for the roughness height of 0.001 mm located at $x_r = 1.0$ mm is about

$$\left(\frac{u_{max}}{q_\infty} \right)_{neutral} = 0.003$$

or $\quad \left(\frac{u_{max}}{U_e} \right)_{neutral} = 0.009$.

In terms of the roughness height, the receptivity coefficient becomes

$$\frac{\left(\dfrac{u_{max}}{U_e} \right)_{neutral}}{\left(\dfrac{h}{\delta} \right)} = 0.66 \ .$$

Similarly, Figs. 7(c) and (d) display the results for the case $\lambda_z = 1.25$ mm case. The initial amplitude of the instability waves in this case is

$$\left(\frac{u_{max}}{q_\infty} \right)_{neutral} = 0.002 .$$

This shows that the receptivity decreased by 1.5 times for the longer wavelength case.

D. Acoustic waves.

After the mean flow was computed, three-dimensional acoustic disturbances were introduced at the outer boundary of the computational domain and time-accurate simulations were performed on the smooth wing surface. Computations were performed with the slow acoustic waves at 0 degrees incidence angle for a frequency of $f = 40$ kHz and for spanwise wavelengths of 1.25 and 1.00 mm. The amplitude of these forced acoustic disturbances was given a small value of $\tilde{p}_{ac}/p_\infty = 1*10^{-5}$ to ensure that the disturbances evolving in the boundary layer remained in the linear regime. The corresponding amplitudes of the acoustic velocity fluctuations are given Table 4. As expected, the amplitudes of the acoustic velocity fluctuations are small compared to the pressure fluctuations.

Table 4. Velocity and pressure fluctuations for the acoustic disturbances

	$\lambda_z = 1.00$	$\lambda_z = 1.25$
$\tilde{u}_{ac}/q_\infty$	$2.88*10^{-7}$	$2.50*10^{-7}$
$\tilde{v}_{ac}/q_\infty$	0.0	0.0
$\tilde{w}_{ac}/q_\infty$	$2.63*10^{-6}$	$2.37*10^{-6}$
$\tilde{p}_{ac}/P_\infty$	$1.0*10^{-5}$	$1.0*10^{-5}$

Figure 8 shows the unsteady density fluctuations at a fixed time obtained from the simulation for the spanwise wavelength of 1.25 mm. Figures 9(a) and (b) depict the maximum *u*-velocity fluctuations generated by the interaction of acoustic disturbances with the wing for this case. Figure 9(a) displays the results in the linear scale, while Fig. 9(b) shows the results in the log scale. Figure 9(a) also displays the freestream acoustic pressure wave to illustrate the difference in the streamwise wavelengths between the incoming acoustic wave and the perturbations generated inside the boundary layer. The insert in Fig. 9(a) shows the expanded view of the fluctuations near leading edge region. We also included the amplitude of the perturbations computed using linear PSE in Fig. 9(b). The agreement is very good between the PSE results and the computations. The maximum amplitude reached is about 0.0005. This is about 400 times smaller than that obtained with the 1μm roughness elements. To obtain the same amplitude of 0.18 as in the roughness case, the freestream acoustic level should be increased to about $\tilde{p}_{ac}/p_\infty = 4*10^{-3}$. This illustrates the inefficiency of acoustic disturbances in generating the traveling crossflow vortices in three-dimensional boundary layers. We calculated the initial amplitude and the receptivity coefficients for the crossflow vortices that are generated by the acoustic waves. The initial amplitude of the instability waves near the neutral point is

$$\left(\frac{u_{max}}{q_\infty}\right)_{neutral} = 1.76*10^{-7}$$

In terms of the acoustic pressure level, the receptivity coefficient becomes

$$\frac{\left(\dfrac{u_{max}}{q_\infty}\right)_{neutral}}{\left(\dfrac{\tilde{p}_{ac}}{p_\infty}\right)} = 1.76*10^{-2} \; .$$

Hence the amplitude of the velocity perturbation of the traveling instability wave generated by the acoustic wave is about 50 times smaller than that of the freestream acoustic pressure level. Similarly, Figs. 10(a) and (b) display the results for the $\lambda_z = 1.00$ mm case. The initial amplitudes of the instability waves in this case is

$$\left(\frac{u_{max}}{q_\infty}\right)_{neutral} = 2.15*10^{-8}.$$

This shows that the receptivity is decreased by 10 times for the shorter wavelength case.

Figure 11 shows the streamwise wavenumber variation along the chordwise direction calculated from the unsteady pressure fluctuations along the wall. This is achieved by first decomposing the fluctuations into harmonic components of the form

$$p(x,z,t) = \tilde{p}(x)e^{i\beta z - i\omega t} + c.c.$$

where c.c. denotes the complex conjugate. The wavenumber of the fluctuations are evaluated from the expression

$$\alpha(x) = (\frac{1}{i\tilde{p}(x)} \frac{\partial \tilde{p}(x)}{\partial x})$$
$$= \alpha_r + i\alpha_i$$

The figure includes the streamwise wavenumber α_r distributions obtained from linear stability computations. The streamwise wavenumber of the slow acoustic wave in the freestream is about -0.0154, is also marked in Fig. 11. As we discussed earlier, the wavelength of the transmitted acoustic waves decreases behind the shock. This is also observed in Fig. 8. The wavenumber near the leading region is about 0.20 compared to the wavenumber of -0.0154 in the freestream. The wavenumber of the pressure perturbations along the surface of the wing first oscillates and decreases from the leading edge. Near $x = 12$ mm, the wavenumber switches to a negative value and merges with the wavenumber for the linear stability wave.

E. Vorticity waves.

Similar to the acoustic case above, three-dimensional vortical disturbances with the following form were introduced at the outer boundary of the computational domain and time-accurate simulations were performed. The conditions imposed are

$$\tilde{v} = 0$$
$$\varepsilon_v = 0$$
$$\tilde{u}/U_\infty = 1 * 10^{-5}$$
$$\tilde{w} = -\alpha_v \tilde{u}/\beta_v$$

where U_∞ is the freestream velocity in the chordwise direction. Computations were performed for the same frequency of $f = 40$ kHz and for spanwise wavelengths of 1.25 and 1.00 mm. The amplitude of these forced vortical disturbances was given a small value of $\tilde{u}_v/U_\infty = 1.0 * 10^{-5}$ to ensure that the disturbances evolving in the boundary layer remained in the linear regime. The amplitudes of the velocity fluctuations for the vorticity waves are given in Table 5. Here the chordwise velocity has the largest magnitude compared to other components.

Table 5. Velocity and pressure fluctuations for the vortical disturbances

	$\lambda_z = 1.00$	$\lambda_z = 1.25$
$\tilde{u}_v / q_\infty$	$1.73*10^{-5}$	$1.73*10^{-5}$
$\tilde{v}_v / q_\infty$	0.0	0.0
$\tilde{v}_v / q_\infty$	$8.83*10^{-6}$	$8.54*10^{-6}$
$\tilde{p}_v / P_\infty$	0.0	0.0

Figure 12 shows the unsteady u-velocity fluctuations obtained from the simulation at a fixed time for the spanwise wavelength of 1.25 mm. Figures 13(a) and (b) give the maximum u-velocity fluctuations generated by the interaction of vortical disturbances with the wing. Figure 13(a) displays the results in the linear scale, while Fig. 13(b) shows the results in the log scale. Similar to the previous case (for the acoustic waves), Fig. 13(a) includes the freestream velocity fluctuations to compare the wavelengths of the freestream and boundary-layer fluctuations. The insert in Fig. 13(a) displays the fluctuations near the leading edge. We also included the amplitude of the perturbations computed using linear PSE in Fig. 13(b). The agreement is very good between the PSE results and the computations. The maximum amplitude reached in this case is about 0.004. This is about 45 times smaller than was obtained with the 1μm roughness elements. Similar to the previous case, to obtain the same amplitude of 0.18 as in the roughness case, the freestream vortical level should be increased to about $\tilde{u}_v / U_\infty = 4.5*10^{-4}$. It is not correct to make a one to one comparison between the amplitudes of disturbances generated by the acoustic and vortical disturbances. However, we can make an observation that the vortical disturbances with $\tilde{u}_v / U_\infty = 1*10^{-5}$ are about eight times more efficient in generating the traveling crossflow vortices than the acoustic waves with $\tilde{p}_{ac} / p_\infty = 1*10^{-5}$. Both are still weak compared to the disturbances generated by 1μm roughness. We calculated the initial amplitude and the receptivity coefficients for the crossflow vortices that are generated by the vorticity waves. The initial amplitude of the instability waves near the neutral points is about

$$\left(\frac{u_{max}}{q_\infty} \right)_{neutral} = 1.16*10^{-6}$$

In terms of the freestream velocity amplitude, the receptivity coefficient becomes

$$\frac{\left(\dfrac{u_{max}}{q_\infty} \right)_{neutral}}{\left(\dfrac{\tilde{u}_v}{q_\infty} \right)} = 6.7*10^{-2} \; .$$

Hence the amplitude of the velocity perturbations of the traveling instability wave generated by the vorticity wave is about 15 times smaller than that of the freestream velocity fluctuations. Similarly, Figs. 14(a) and (b) display the results for the case $\lambda_z = 1.00$ mm case. The initial amplitudes of the instability waves in this case is

$$\left(\frac{u_{\max}}{q_\infty} \right)_{neutral} = 1.51*10^{-7}.$$

This demonstrates that the receptivity decreased by 8 times for the shorter wavelength case.

We performed the simulations with increasing freestream levels. We present the maximum u-velocity fluctuations obtained with $\tilde{u}_v/U_\infty = 1*10^{-3}$ in Fig. 13(b). The amplitudes levels are about 100 times larger than that obtained with $\tilde{u}_v/U_\infty = 1*10^{-5}$. The amplitudes saturate around 0.18, approximately the same as that for the stationary case shown in Figs. 7(b) and (d). The growth rate deviates from the linear stability results at about $x = 33$ mm. Figure 15 displays the u-velocity contours in the cross-sectional planes (z, y) at different stations, $x = 13.96, 23.50, 31.60$ and 42.40 mm, along the wing. Similar to the stationary crossflow case (Fig. 6), the traveling crossflow vortices amplify downstream and develop strong shear layers, although unsteady, in both the normal and the spanwise directions. However, it is interesting to observe that the roll up of vortices is more confined towards the wall and more elongated in the spanwise direction compared to the stationary case.

Similar to the acoustic wave case, Fig. 11 shows the streamwise wavenumber variation along the chordwise direction calculated from the unsteady pressure fluctuations along the wall. The streamwise wavenumber of the vorticity wave in the freestream is about -0.069 and is also included in Fig. 11. As we discussed earlier, the wavelength of the transmitted waves decreases behind the shock. This is also observed in Fig. 12. The wavenumber of the pressure perturbations along the surface of the wing first oscillates and near $x = 12$ mm, this wavenumber merges with the wavenumber of the linear stability wave.

F. Interaction of stationary and traveling waves.

After separately investigating the generation of stationary and traveling crossflow instability waves by the roughness, acoustic and vortical disturbances, we consider the interaction of stationary and traveling waves in this section. We performed the computations for a fixed roughness height with increasing freestream turbulence levels of $\tilde{u}_v/U_\infty = 1.0*10^{-4}$, $1.0*10^{-3}$ and $1.0*10^{-2}$. The roughness height and location are the same as given in Section C and Table 3. The roughness is located at $x_r = 1.0$ mm and the roughness height is $h = 0.001$ mm. The simulations are performed for a spanwise wavelength of 1.25 mm. The distribution and frequency of the vortical disturbances are the same as described in Section E. The frequency of the vortical disturbances is 40 kHz. It is to be noted that the initial amplitude of the stationary crossflow vortex for the roughness height of 0.001 mm is 0.002 and the amplitude of the traveling crossflow vortex generated by the vorticity wave with the freestream amplitude level of $1.0*10^{-5}$ is $1.16*10^{-6}$. Hence, the expected initial amplitudes of the traveling crossflow vortices will be $1.16*10^{-5}$, $1.16*10^{-4}$ and $1.16*10^{-3}$ for the increasing freestream amplitudes of $1.0*10^{-4}$, $1.0*10^{-3}$ and $1.0*10^{-2}$, respectively. The initial amplitudes of the traveling waves are on the order of 100 and 10 times smaller than that for the stationary vortex for the freestream amplitude levels of $1.0*10^{-4}$ and $1.0*10^{-3}$ and they are of the same order at the highest amplitude level of $1.0*10^{-2}$.

Figures 16 and 17 show the results qualitatively and Figs. 18-20 depict the results quantitatively. Figure 16 shows the unsteady u-velocity fluctuations obtained from the simulation at a fixed time with the roughness and the freestream vortical disturbances. The results are shown for the case with the medium freestream amplitude level of $\tilde{u}_v/U_\infty = 1*10^{-3}$. Compared to Figs. 12(a) and (b), we observe the strong perturbations induced by the roughness inside the boundary layer and the vortical disturbances outside the boundary layer are essentially unchanged. Figures 17(a-d) give the instantaneous u-velocity contours in the cross-sectional planes (z, y) at a fixed station $x = 31.60$ mm for the four cases: (a) roughness only, and (b), (c) and (d) roughness and vortical disturbances with increasing amplitude levels of $1.0*10^{-4}$, $1.0*10^{-3}$ and $1.0*10^{-2}$, respectively. It is interesting to see that the velocity contours are almost the same in Figs. 17(a), (b) and (c). This implies that at the small and medium freestream amplitude levels of $1.0*10^{-4}$ and $1.0*10^{-3}$ where the initial amplitude levels of the traveling waves are much smaller than that for the

stationary disturbances, the traveling waves do not inhibit or modify the development of the stationary vortices, which dominate the perturbation field. The velocity contours in Fig. 17(d) differ dramatically from Fig. 17(a). The remnants of the stationary vortices are not clearly visible in this figure. This suggests that in this case where the initial amplitudes of the traveling and the stationary waves are comparable, the traveling disturbances dominate the perturbation field and the growth of the stationary vortices are inhibited by the growing traveling waves.

To evaluate the evolution of stationary and traveling disturbances along the chordwise direction, we decompose the computed perturbation field into Fourier modes using Fast Fourier Transforms (FFT). The velocity field $u(x,y,z,t)$ is decomposed as

$$u(x,y,z,t) = \sum_{m=-M}^{M-1} \sum_{n=-N}^{N-1} \tilde{u}_{m,n}(x,y)\, e^{im\beta z - in\omega t}$$

where the spanwise wavenumber β and the frequency ω correspond to the longest spanwise wavelength of $\lambda_z = 1.25$ mm, and the smallest frequency of 40 kHz. $\tilde{u}_{m,n}(x,y)$ is the amplitude function for the Fourier mode $(m\beta, n\omega)$. The results are presented in terms of the spanwise-frequency mode number (m,n). Hence, mode (1,0) represents the primary stationary crossflow vortex mode with the spanwise wavelength of $\lambda_z = 1.25$ mm and the mode (1,1) denotes the primary traveling mode with the spanwise wavelength of 1.25 mm and the frequency of 40 kHz. Similarly, mode (0,0) denotes the meanflow distortion and (0,2), (1,2), etc. denote the higher modes generated by the nonlinear interactions. Figures 18(a-d) display the evolution of the maximum amplitude of the streamwise velocity $(\tilde{u}_{m,n}(x,y))_{max}$ of different modes for the four cases: (a) stationary vortex only and (b), (c) and (d) stationary and traveling vortices with increasing freestream amplitudes of $1.0*10^{-4}$, $1.0*10^{-3}$ and $1.0*10^{-2}$, respectively. The evolution of the primary modes (1,0) and (1,1) are denoted in these figures by the solid red and blue curves, respectively. Figure 18(a) depicts the growth and the saturation of the primary stationary vortex (1,0) and the generation of higher modes (0,0) and (2,0) due to nonlinear interactions. The primary stationary mode saturates at an amplitude of 0.09 near $x = 30$ mm and remains at that level further downstream. The meanflow distortion and the higher harmonic also saturate around $x = 30$ mm and remain at that level further downstream. These observations agree qualitatively with previous calculations[6] using PSE in incompressible flows. Figures 18(b) and (c) show the evolution of different modes for the interaction cases with freestream amplitude levels of $1.0*10^{-4}$ and $1.0*10^{-3}$, respectively. First observation is that the initial amplitudes of the traveling modes in these cases are, as mentioned earlier, much lower than that for the stationary modes. More importantly, the evolution and saturation of the primary stationary mode in these cases are the same as in Fig. 18(a). The traveling modes grow initially and reach a maximum value near $x = 25$ mm and then decay before growing again further downstream. The maximum amplitudes attained by the traveling modes are still at least one order of magnitude smaller than those of the stationary modes. In contrary to the previous cases, when the initial amplitudes of the stationary and traveling waves are comparable, the picture changes as displayed in Fig. 18(d). The first observation is that the evolution of the primary stationary vortex is significantly modified by the traveling modes. The growth of the stationary mode is suppressed. The stationary mode reaches a maximum amplitude of 0.02 near $x = 15$ mm compared to 0.09 in the previous cases. Similarly, the amplitude of the steady higher mode (2,0) also remains lower than in the previous cases. The suppression of the stationary modes and the increased presence of the traveling modes help to explain the velocity contours that we observed in Fig. 17(d).

To compare the evolution of the primary modes in all four cases, we plotted the amplitudes of the primary stationary (1,0) and traveling (1,1) modes for the four cases in Fig. 19. It is seen that except for the highest amplitude case, the evolution of the stationary vortex is not affected by the traveling mode. Secondly, the amplitudes of the traveling modes remain at least an order of magnitude smaller than that of the stationary mode for all but the largest vortical amplitude. When the initial amplitudes of the

stationary and the traveling modes are comparable, the growth of the stationary mode is suppressed and the amplitudes of traveling modes are larger than that of the stationary mode. These conclusions agree with the experimental observations of Bippes[4] for incompressible flows.

Figures 20(a-c) show the chordwise velocity profiles at different spanwise positions $z = [0, \lambda_z]$ at the chordwise positions $x = 31.6$ mm for the cases (a) and (c) and at $x = 42.4$ mm for the case (b). Figure 20(a) depicts the results for the roughness case only, Fig. 20(b) displays the profiles for the traveling waves only with the freestream vortical disturbance amplitude of $1.0*10^{-3}$, and Fig. 20(c) shows the results for the interaction case with the roughness and freestream amplitude of $1.0*10^{-2}$. In the last two cases, the instantaneous profiles at a fixed time are plotted. Figure 20(a) displays the typical velocity profiles generated by the nonlinear stationary crossflow vortices. They also have been observed in experiments[4,5] and in computations.[6,8] These profiles are highly inflectional near the edge of the boundary layer and are the impetus for the secondary instability that leads to final breakdown to turbulence for these vortices.[4,5,6,7,8] Figure 20(b) shows the profiles formed by the traveling modes. These profiles also consist of inflection points. However, compared to the stationary case, they do not spread to the outer edge of the boundary layer and the gradients near the inflections points are weaker than those in the stationary case. Figure 20(c) shows the results in the interaction case. This is a strongly nonlinear region and the profiles are perturbed more near the wall region compared to the edge of the boundary layer. The important question is how do these profiles enhance or suppress the secondary instability and the final breakdown to turbulence. This is not attempted in this work and needs further analysis.

IV. Summary and Conclusions

We investigated the receptivity, growth and interaction of stationary and traveling crossflow instability waves in a supersonic flow over a blunt biconvex swept wing. The chord length of the model is 150 mm and the maximum thickness is 30 mm. The simulations were performed at a freestream Mach number of 3.0, a sweep angle of 30 degrees and a unit Reynolds number of $18.0*10^6$/m. The model and the flow parameters are the same as those in the experiments of Archambaud et al.[10] The measured transition location on this model for these conditions occurred near $x = 45$ mm. The simulations were performed by solving the three-dimensional Navier-Stokes equations using a 5th-order accurate weighted essentially non-oscillatory (WENO) scheme for space discretization and using a 3rd-order, total variation diminishing (TVD) Runge-Kutta scheme for time integration. The receptivity and evolution of stationary crossflow vortices were studied by performing the simulations with three-dimensional roughness elements of particular spanwise wavelength placed near the leading edge of the wing. The receptivity of traveling crossflow vortices to acoustic and vortical external disturbances were investigated by performing time accurate simulations with acoustic and vortical three-dimensional waves of particular frequency and spanwise wavelength superimposed on the incoming freestream at the outer boundary of the computational domain. Additionally, the interaction of stationary and traveling crossflow vortices were studied by performing the simulations with the roughness elements placed near the leading edge and vortical disturbances of increasing amplitudes superimposed on the incoming freestream.

The meanflow profiles show that the maximum crossflow velocity remains almost at a constant value of 7% of the freestream velocity starting from the leading edge. This is reflected in a large crossflow Reynolds numbers near the leading edge. The neutral points of the stationary and traveling disturbances are located within 2.5% of the chord. All linear stability computations were performed for constant spanwise wavelengths and show that the N-Factors at the measured transition onset location[10] are about 6.5 for traveling disturbances and about 4.8 for stationary disturbances.

The receptivity analysis yielded that the initial amplitudes of the stationary crossflow vortices originating from 1μm three-dimensional roughness elements located near the neutral points are about 0.003 and 0.002 for spanwise wavelengths of 1.00 and 1.25 mm, respectively. The simulations show that the crossflow vortices initially grow according to linear theory and saturates at an amplitude of about 18% of the freestream velocity. The flow features and the evolutions of these vortices resemble experimental

and computational results observed in incompressible flows. The initial amplitudes of the traveling vortices generated by the freestream acoustic disturbances with pressure amplitude level of $\tilde{p}_{ac}/p_\infty = 1.0*10^{-5}$ are $1.76*10^{-7}$ and $2.15*10^{-8}$ for spanwise wavelengths of 1.25 and 1.00mm, respectively. Similarly, the initial amplitudes of the traveling modes generated by vortical disturbances with velocity amplitude level of $\tilde{u}_v/U_\infty = 1*10^{-5}$ are $1.16*10^{-6}$ and $1.51*10^{-7}$. It is not correct to make a one to one comparison of the initial amplitudes generated by roughness, acoustic and vortical disturbances. However, the results show that the stationary vortices generated by the 1μm roughness is about 2000 times larger than the traveling disturbances generated by the vortical waves. Additionally, the acoustic disturbances are about 8 times weaker in generating unstable traveling crossflow vortices compared to the vorticity waves.

The simulation of the interaction of stationary and traveling crossflow vortices show that as long as the initial amplitudes of the stationary crossflow vortices are large compared to the traveling vortices, the growth and the evolution of the stationary vortices are neither suppressed or modified. When the initial amplitudes of the stationary and traveling waves are comparable, due to the larger growth rate of the traveling vortices compared to the stationary waves, the traveling disturbance dominates the perturbation field. The growth of the stationary vortices is suppressed by the growing traveling wave. The modified velocity profiles exhibit highly inflectional character. It is known that these highly inflectional profiles are susceptible to high-frequency strong secondary instabilities. We have not addressed this third element of the transition process in this paper. Namely, how do these profiles enhance or suppress the secondary instability and the final breakdown to turbulence. This was not attempted in this work and needs further analysis.

References

1. Arnal, D. "Boundary Layer Transition: Predictions Based on Linear Theory," Progress in transition modeling, AGARD Rep. No. 793, 1994.

2. Reed, H. L., and Saric, W. S., "Linear Stability Theory Applied to Boundary Layers," Annual Review of Fluid Mechanics, Vol. 28, pp. 389-428, 1996.

3. Malik, M. R., "Boundary-Layer Transition Prediction Toolkit," AIAA Paper 1997-1904, 1997.

4. Bippes, H., "Basic experiments on transition in three-dimensional boundary layers dominated by crossflow instability," *Progress in Aerospace Sciences*, Vol. 35, pp. 363-412, 1999.

5. Saric, W. S., Reed, H. L., and White, E. B., "Stability and Transition of Three-Dimensional Boundary Layers," *Annual Review of Fluid Mechanics*, Vol. 35, pp. 413-440, 2003.

6. Malik, M., Li, F., and Chang, C., "Crossflow disturbances in three-dimensional boundary layers; Nonlinear development, wave interaction and secondary instability," *Journal of Fluid Mechanics*, Vol. 268, pp. 1-36, June 1994.

7. Malik, M., Li, F., Choudhari, M. M., and Chang, C., "Secondary instability of crossflow vortices and swept-wing boundary-layer transition," *Journal of Fluid Mechanics*, Vol. 399, pp. 85-115, 1999.

8. Wassermann, P., and Kloker, M., "Mechanisms and passive control of crossflow-vortex-induced transition in a three-dimensional boundary layer," *Journal of Fluid Mechanics*, Vol. 456, pp. 49-84, 2002.

9. Balakumar, P., and King, R. A., "Receptivity and Transition of Supersonic Boundary Layers Over Swept Wings," AIAA Paper 2010-1454, 2010.

10. Archambaud, J. P., Louis, F., Séraudie, A., Arnal, D. and Carrier, G., "Natural Transition in Supersonic Flows: Flat Plate, Swept Cylinder, Swept Wing," AIAA Paper 2004-2245, 2004.

11. Shu, Chi-Wang, " Essentially Non-Oscillatory and Weighted Essentially Non-Oscillatory Schemes for Hyperbolic Conservation Laws," *NASA/CR-97-206253 and ICASE Report* No. 97-6, 1997.

12. Atkins, H. L., "High-Order ENO Methods for the Unsteady Compressible Navier-Stokes Equations," AIAA Paper 1991-1557, 1991.

13. Balakumar, P., Zhao, H., and Atkins, H., "Stability of Hypersonic Boundary Layers Over a Compression Corner," AIAA Paper 2002-2848, 2002.

American Institute of Aeronautics and Astronautics

$$p = p_{ac}\, e^{i\alpha x + i\beta z - i\omega t} \quad \text{Acoustic}$$

$$v = v_{v}\, e^{i\alpha x + i\beta z - i\omega t} \quad \text{Vorticity}$$
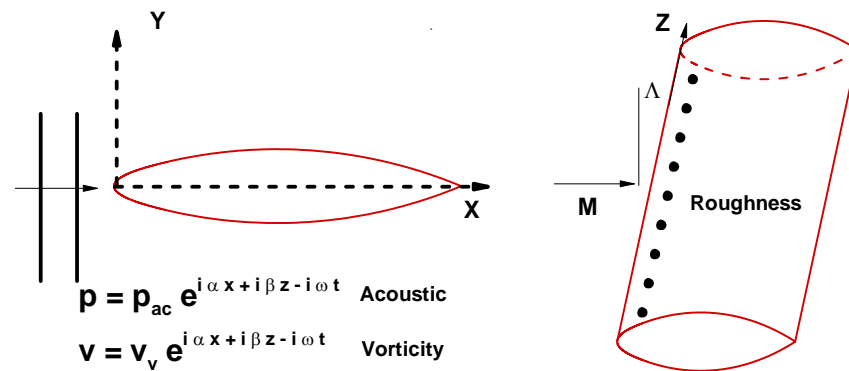
Figure 1. Supersonic flow over an infinite biconvex blunt wing.
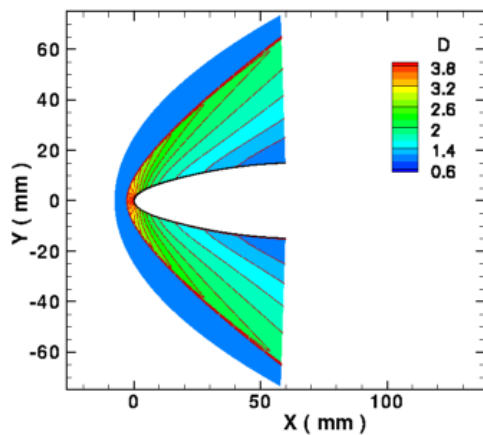
Figure 2. Contours of density for flow over an infinite swept wing with a blunt leading edge at M = 3.0.
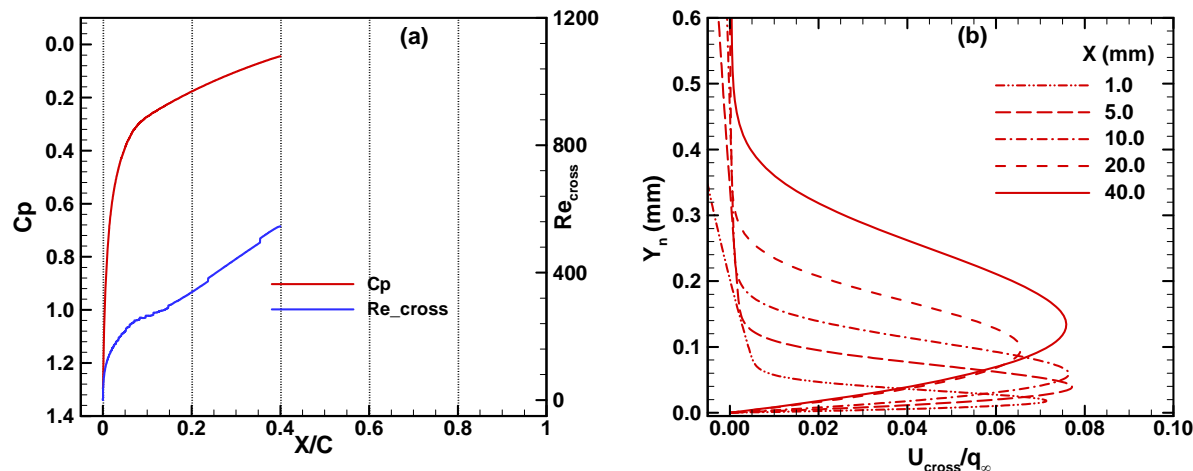
Figure 3. Computed (a) pressure distribution and the crossflow Reynolds number along the wing and (b) the crossflow velocity profiles at different stations.
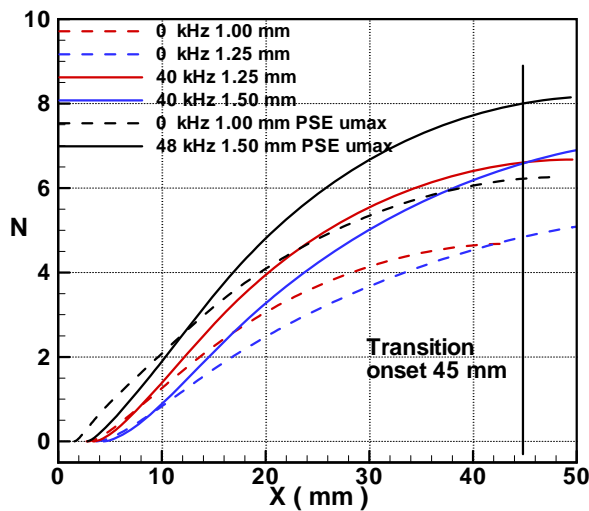
Figure 4. N-factors computed from local stability and linear PSE methods for the stationary and traveling disturbances.
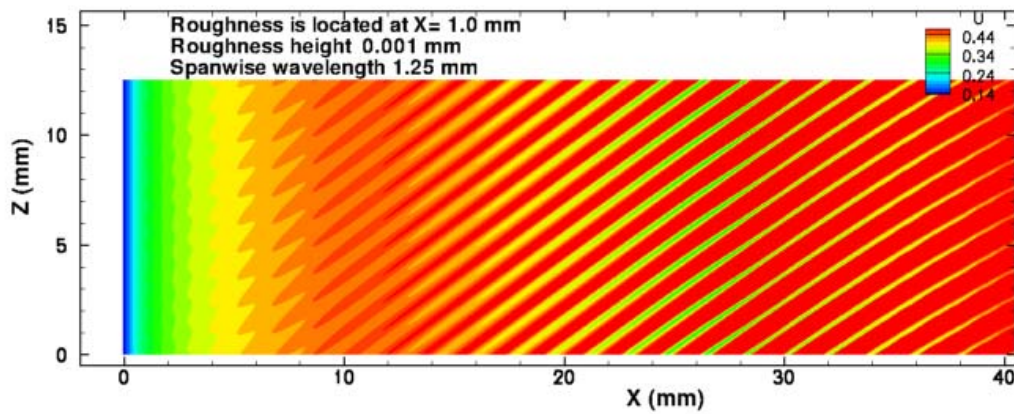
Figure 5. Contours of the *u* velocity in the plan view (*x*, *z*) plane.
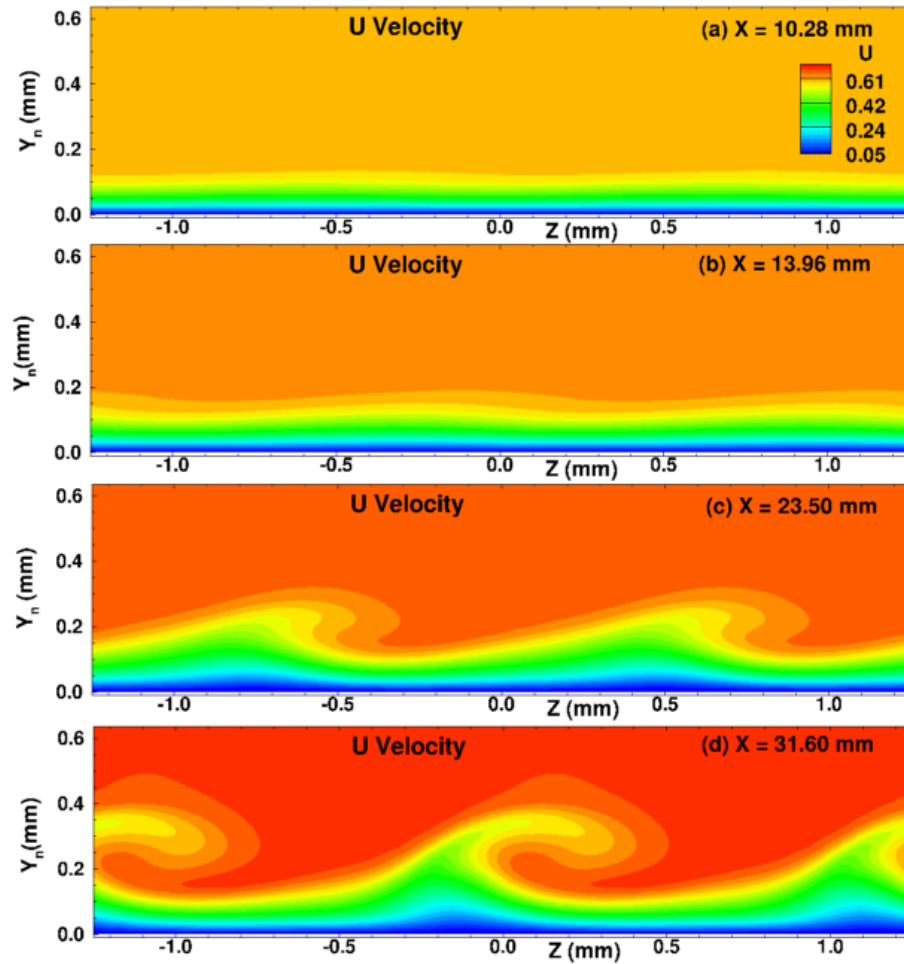
Figure 6. Contours of the _u_ velocity generated by the roughness elements in the cross-sectional planes (y, z) at chordwise stations of x = 10.28, 13.96, 23.50 and 31.60 mm (λ_z = 1.25 mm, h = 0.001 mm).
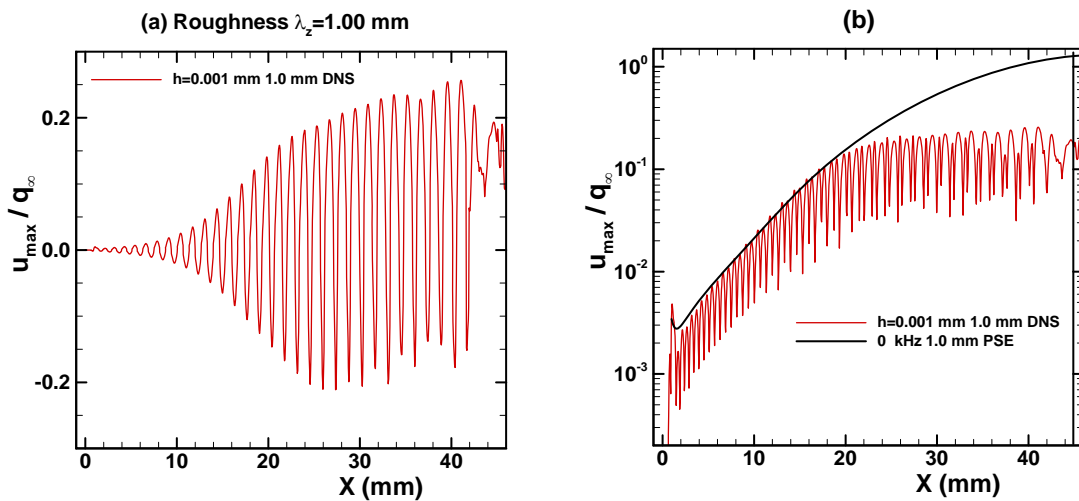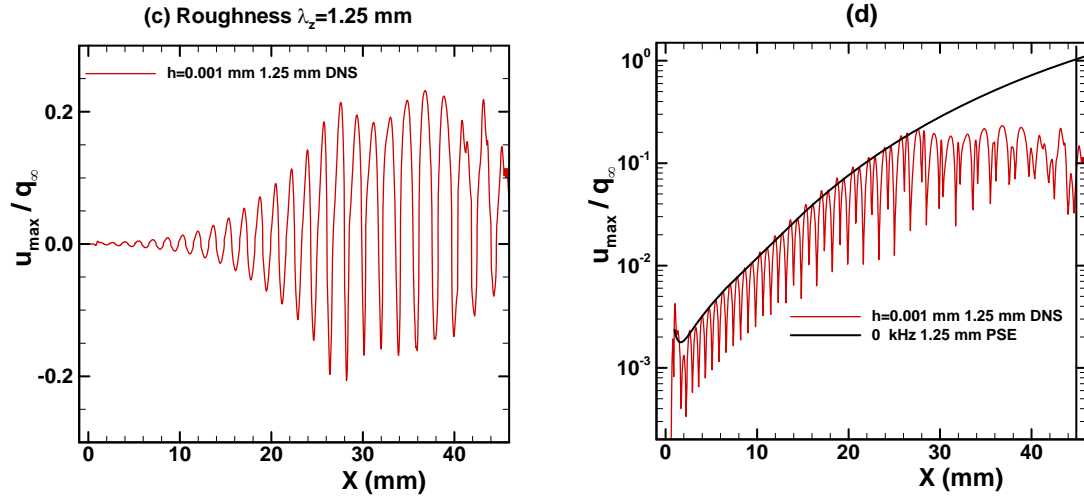
Figure 7. Perturbations of the maximum *u*-velocity component generated by the roughness and PSE results along the wing for $\lambda_z = 1.00$ mm and $\lambda_z = 1.25$ mm ((a) & (c) in linear scale, (b) & (d) in log-scale).
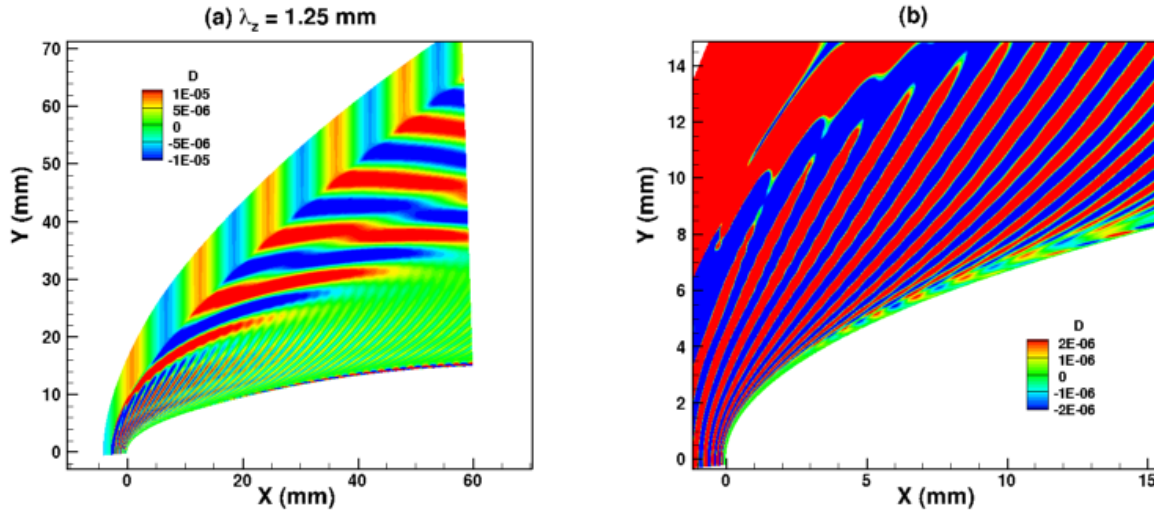
Figure 8. Density fluctuations generated by the interaction of acoustic waves with the blunt swept wing ($f = 40$ kHz, $\lambda_z = 1.25$ mm, $\tilde{p}_{ac}/p_{\infty} = 1.0*10^{-5}$).
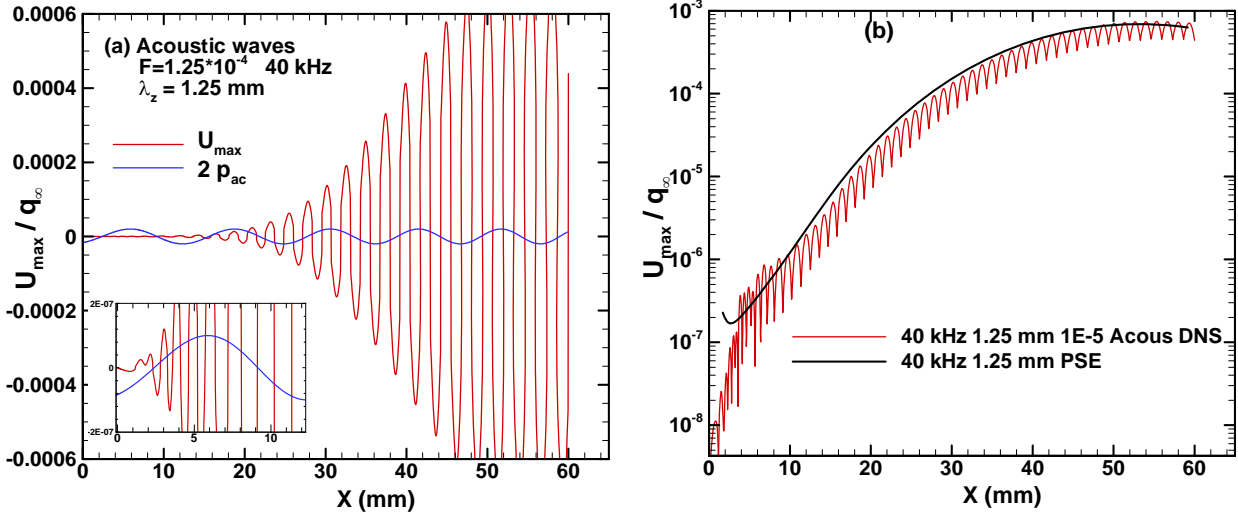
Figure 9. Perturbations of the maximum u-velocity component along the blunt wing generated by the acoustic waves (a) in linear scale (b) in log-scale (f = 40 kHz, λ_z = 1.25 mm, $\tilde{p}_{ac}/p_\infty = 1.0*10^{-5}$).
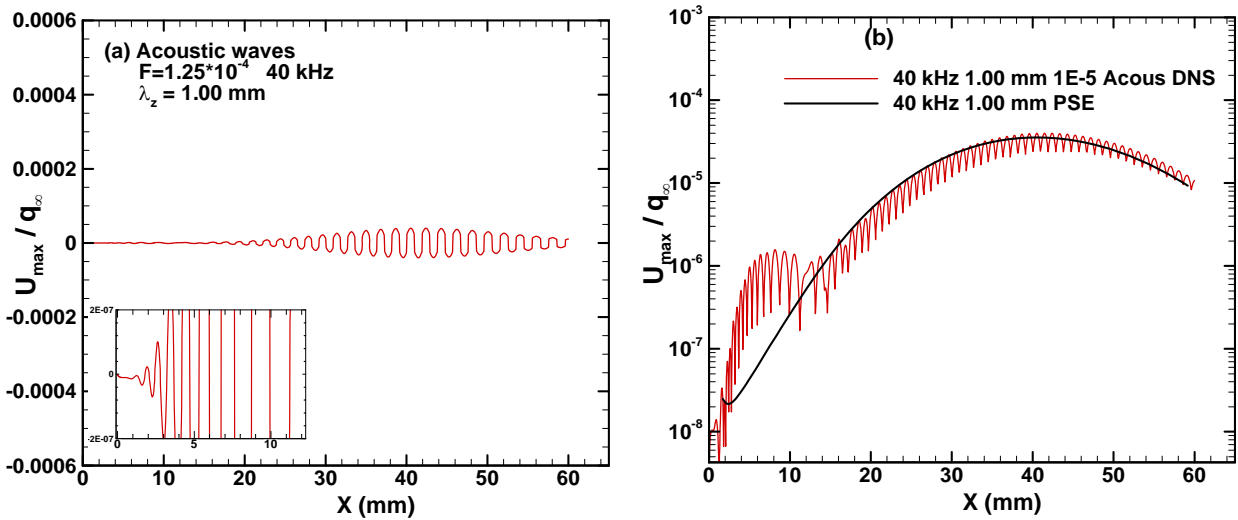
Figure 10. Perturbations of the maximum u-velocity component along the blunt wing generated by the acoustic waves (a) in linear scale (b) in log-scale (f = 40 kHz, λ_z = 1.00 mm, $\tilde{p}_{ac}/p_\infty = 1.0*10^{-5}$).
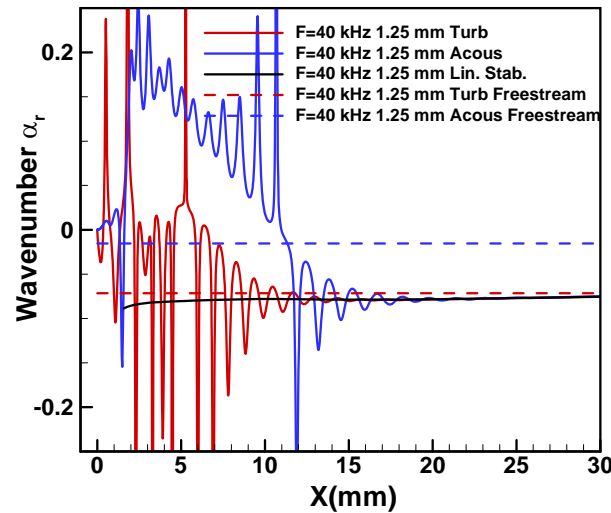
Figure 11. Wavenumbers of the pressure fluctuation along the wall generated by the acoustic and vortical disturbances and comparison with the linear stability (f = 40 kHz, λ_z = 1.25 mm).
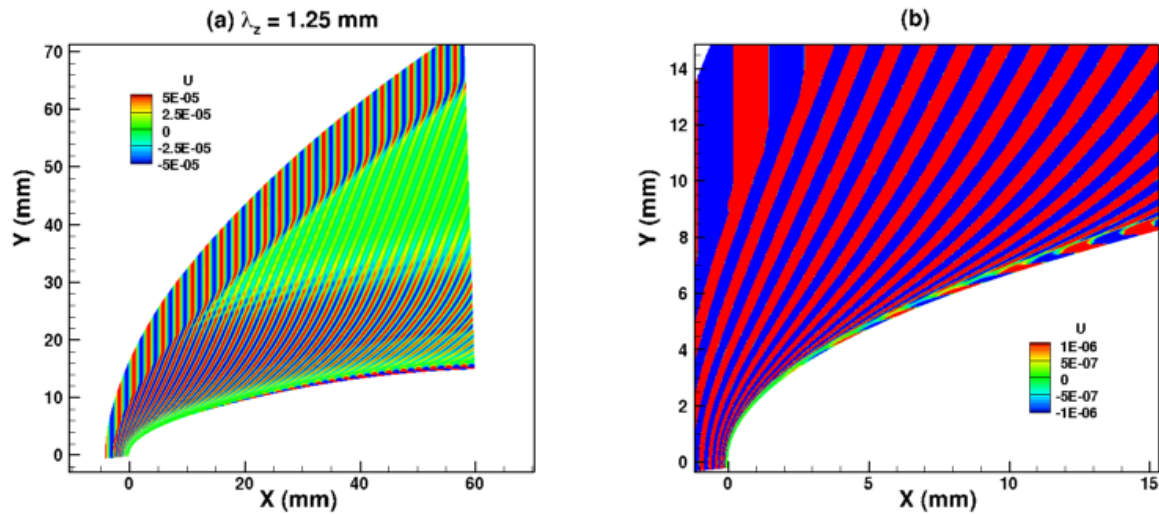
Figure 12. u-velocity fluctuations generated by the interaction of vorticity waves with the blunt swept wing (f = 40 kHz, λ_z = 1.25 mm, $\tilde{u}_v / U_\infty$ = 1.0*10^{-5}).

Figure 13. Perturbations of the maximum *u*-velocity component along the blunt wing generated by the vorticity waves (a) in linear scale (b) in log-scale (f = 40 kHz, λ_z = 1.25 mm, $\tilde{u}_v/U_\infty$ = 1.0*10^{-5}).
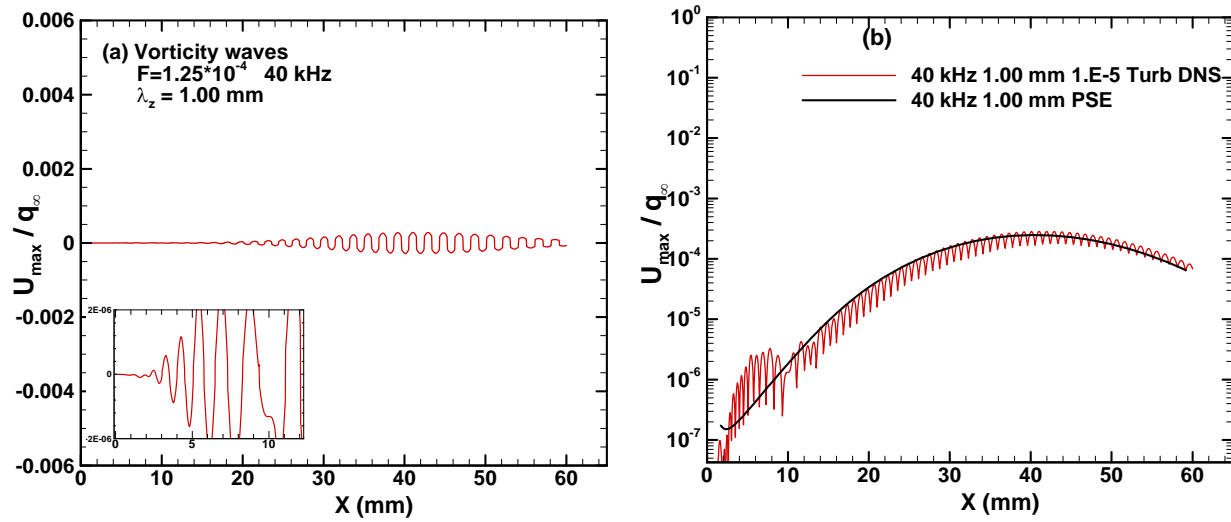
Figure 14. Perturbations of the maximum *u*-velocity component along the blunt wing generated by the vorticity waves (a) in linear scale (b) in log-scale (f = 40 kHz, λ_z = 1.00 mm, $\tilde{u}_v/U_\infty$ = 1.0*10^{-5}).
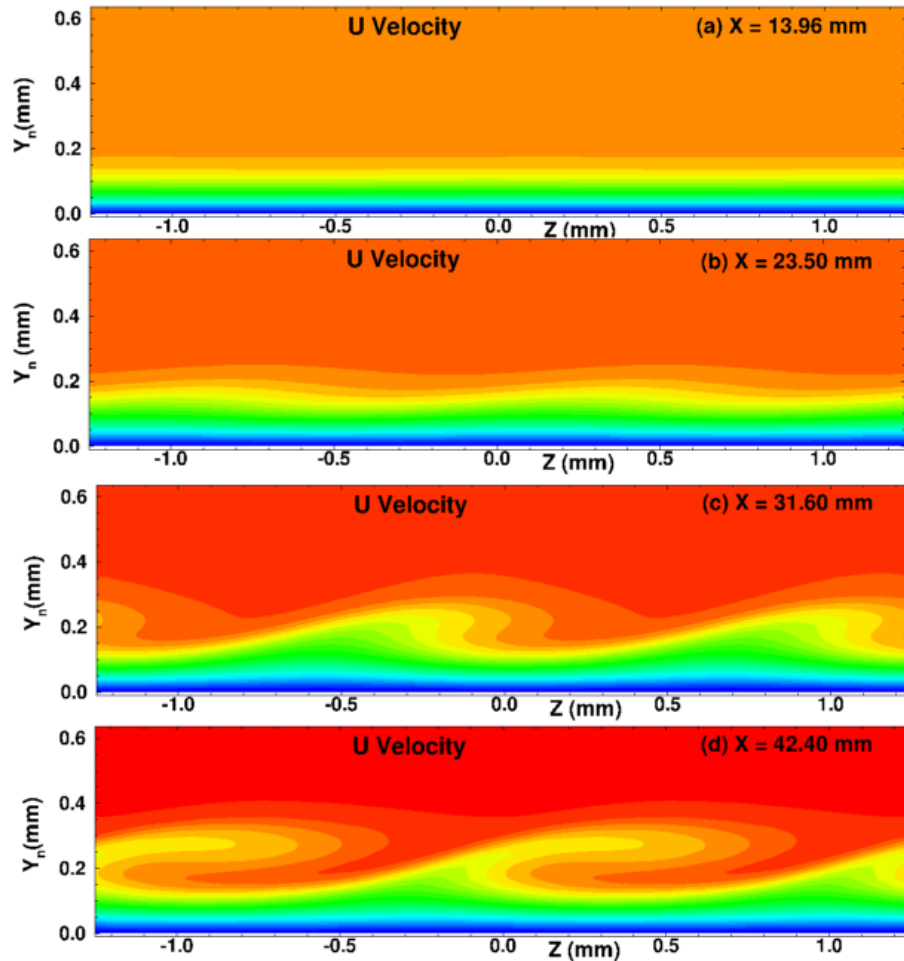
Figure 15. Contours of the *u* velocity in the cross-sectional planes (*y, z*) generated by the vorticity wave at chordwise stations of *x* = 13.96, 23.50, 31.60 and 42.40 mm (*f* = 40 kHz, λ_z = 1.25 mm, $\tilde{u}_v / U_\infty$ = 1.0*10^{-3}).
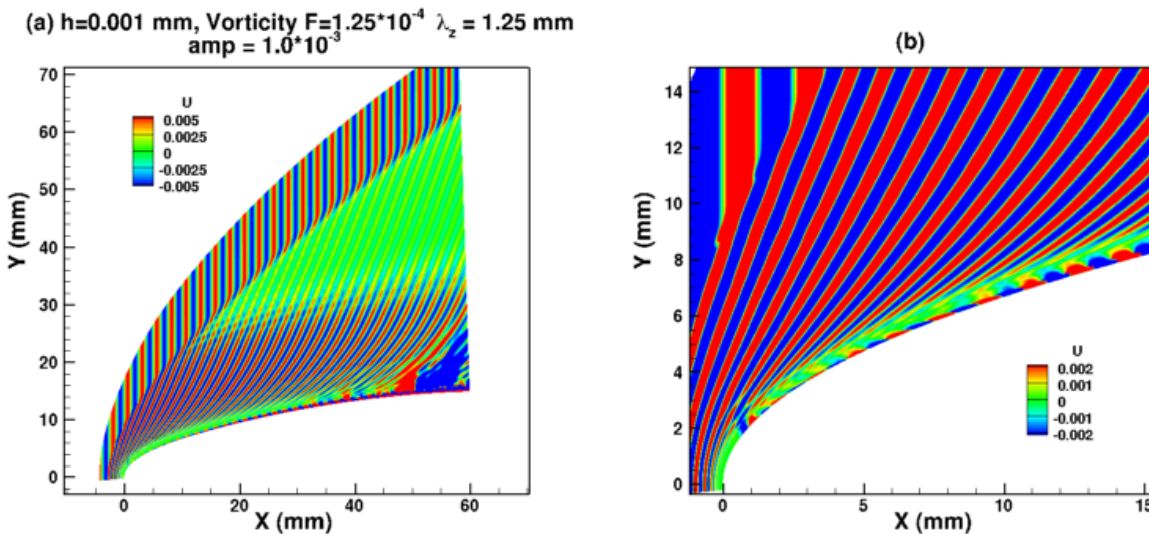
Figure 16. *u*-velocity fluctuations generated by the interaction of vorticity waves and roughness (*h* = 0.001 mm, *f* = 40kHz, λ_z = 1.25 mm, $\tilde{u}_v / U_\infty$ = 1.0*10^{-3}).
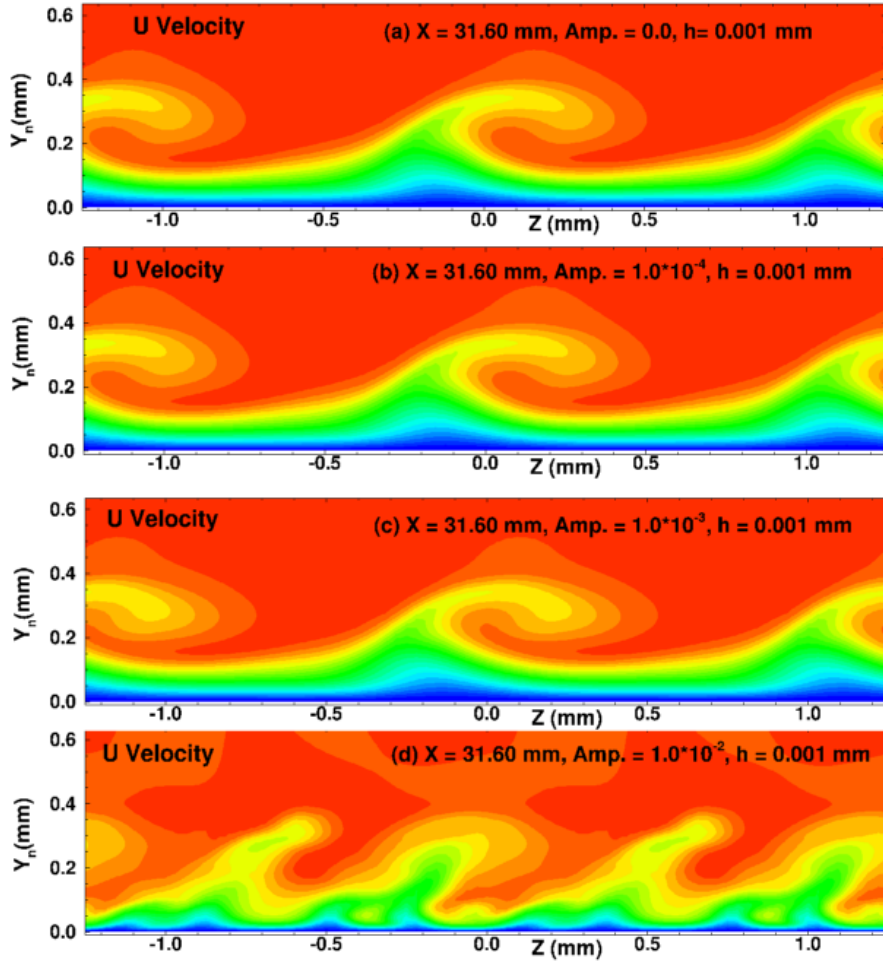
Figure 17. Contours of the *u* velocity generated by the interaction of vorticity waves and roughness in the cross-sectional planes (*y*, *z*) at *x* = 31.60 mm (h = 0.001 mm, *f* = 40 kHz, λ_z = 1.25 mm) for (a) roughness only and for (b), (c) and (d) roughness and freestream vorticity waves with increasing amplitudes of $\tilde{u}_v / U_\infty$ = 1.0*10⁻⁴, 1.0*10⁻³ and 1.0*10⁻², respectively.

American Institute of Aeronautics and Astronautics
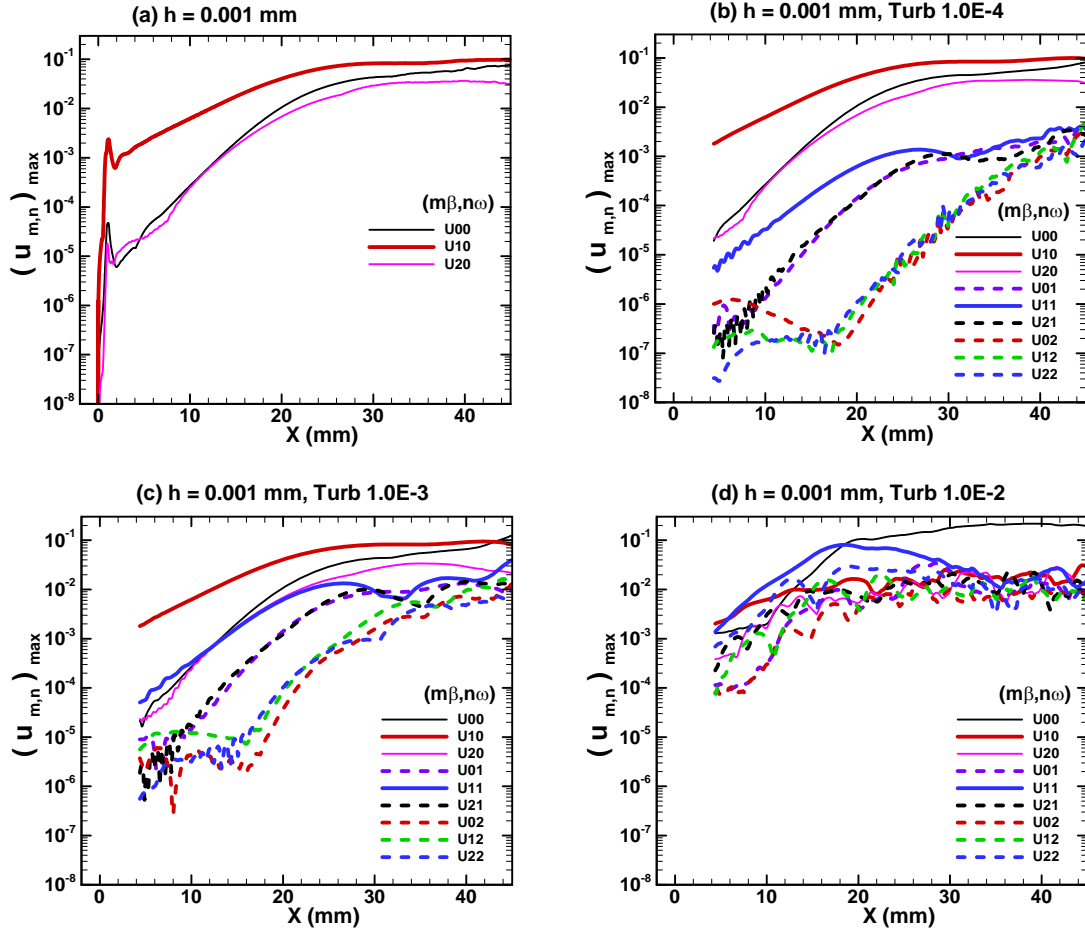
Figure 18. Evolution of the maximum streamwise velocity for different Fourier modes (mβ, nα) generated by the interaction of vorticity waves and roughness (h = 0.001 mm, f = 40 kHz, λ_z = 1.25 mm): (a) roughness only (b), (c) and (d) roughness and vorticity waves with increasing amplitudes of $\tilde{u}_v / U_\infty$ = 1.0*10^{-4}, 1.0*10^{-3} and 1.0*10^{-2}.
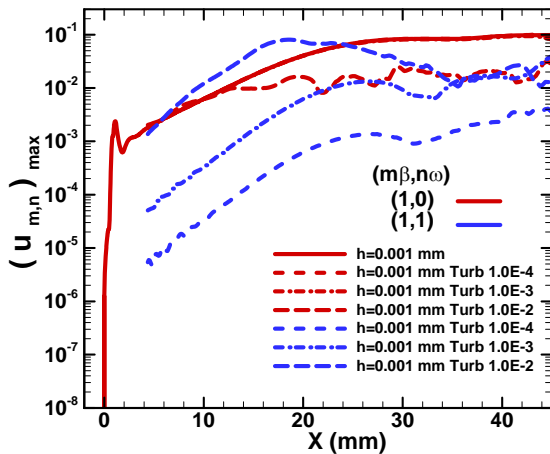

Figure 19. Evolution of the maximum streamwise velocity for the primary modes (1,0) and (1,1) generated by the interaction of vorticity waves and roughness.
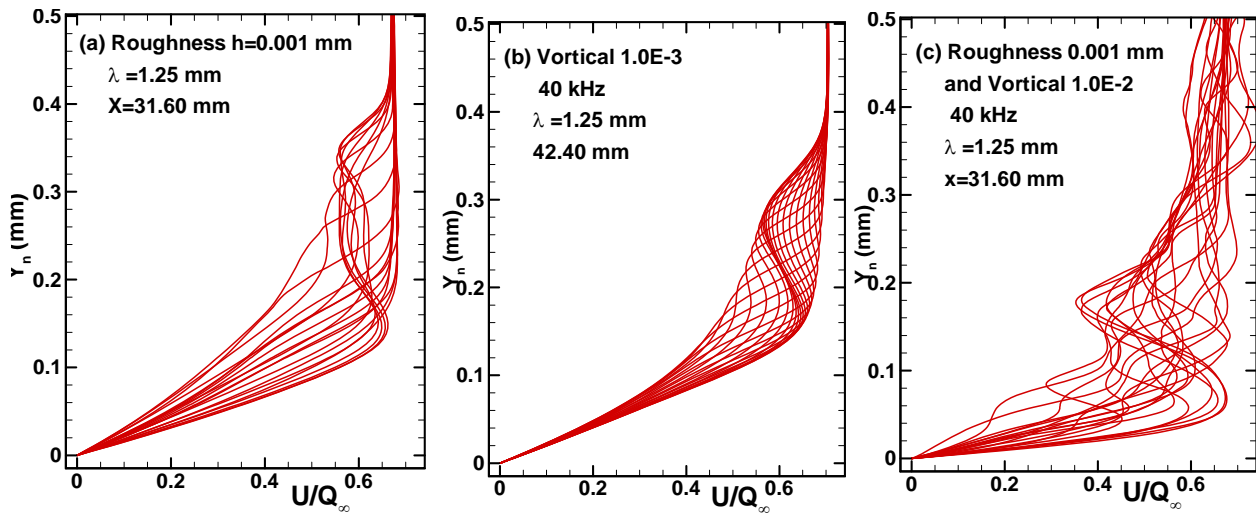
Figure 20. Instantaneous streamwise velocity profiles at different spanswise locations $z = [0, 1.25$ **mm]** and chordwise stations: (a) roughness only ($h = 0.001$ mm, $x = 31.60$ mm), (b) vorticity wave only ($\tilde{u}_v / U_\infty = 1.0*10^{-3}$, $x = 42.40$ mm) and (c) interaction of both roughness and vorticity waves ($h = 0.001$ mm, $\tilde{u}_v / U_\infty = 1.0*10^{-2}$, $x = 31.60$ mm).